Organic Process Research & Development

ARTICLE

pubs.acs.org/OPRD

Reactor Kinetics Studies via Process Raman Spectroscopy, Multivariate Chemometrics, and Kinetics Modeling

Melissa Assirelli, Weiyin Xu, and Wee Chew*

Institute of Chemical and Engineering Sciences (ICES), Agency for Science, Technology and Research (A*STAR), 1 Pesek Road, Jurong Island, Singapore 627833, Singapore

Supporting Information

ABSTRACT: The deployment of in situ analytics for monitoring chemical reactions in process chemistry development and scale-up is facilitated by advanced instrumentation such as Raman spectrometry. Furthermore, greater process understanding can be engendered by coupling in situ Raman data with multivariate chemometrics analyses and kinetics modeling. Such information is important for devising science-based process control strategies along the concept of quality by design (QbD) initiated through the U.S. FDA process analytical technology (PAT) framework. A series of experiments using varied glass reactors, stirring speeds, and isothermal reaction temperatures were designed with acetic anhydride hydrolysis as the model reaction to successfully demonstrate the efficacy of combining in situ Raman spectroscopy, multivariate analyses, and kinetics modeling. Two different Raman measurement methods, using immersion and noncontact probe optics, were tested through a process Raman spectrometer with multiplexing capability. Information-theoretic multivariate chemometrics were applied to elicit pure component spectra and transient concentrations of chemical species, and two differential-algebraic equations modeling approaches were adopted for elucidating chemical and dissolution kinetics information. The variations in reactor vessel type and sizes, stirring speeds, Raman measurements, and kinetics models were compared in this study.

INTRODUCTION

Raman spectroscopy has proliferated into diverse applications[1−4] since the landmark experimental discoveries in the late 1920s by Raman and Krishnan[5] and Landsberg and Mendelstam.[6] The application of Raman spectroscopy in industrial scenarios has been of great interest of late due to first advancement in fiber optics technology[7] and process Raman instrumentation design,[8−11] and second the introduction of Process Analytical Technology (PAT) guidelines from the United States Food and Drug Administration (FDA).[12,13] To date, Raman spectroscopy has been implemented in the chemical, biochemical, and pharmaceutical industries for online monitoring of reactions, distillation processes, fermentations, polymer morphology, semiconductor fabrication and quality assurance,[11,14] and studying polymorphic transformations, crystallization, and formulations.[14−16]

The FDA PAT initiative promotes the enlargement and adoption of innovative approaches to pharmaceutical development, manufacturing, and quality assurance[12] alongside FDA Pharmaceutical cGMP guidelines for the 21st century.[17] This led to active deliberations in various related issues and methodological concepts such as design of experiment (DoE), design space, criticality, control strategy, quality risk management, quality by design (QbD), and real time release (RTR).[13] Many of these concepts and related methodologies were also raised by the European Medicines Agency (EMA) PAT team in 2006[18] and in the more recent Product Quality Lifecycle Implementation (PQLI) initiative in 2007 by the International Society for Pharmaceutical Engineering (ISPE).[19] The PQLI initiative is for the practical implementation of the International Conference on Harmonisation (ICH) tripartite guideline Q8 (R2), Q9, and Q10.[19] *Process understanding* is the common thread that strings the aforesaid PAT related issues, which implies in-depth knowledge about product Critical Quality Attributes (CQAs), Critical Process Parameters (CPP), and sources of variability associated with the pharmaceutical operations unit. In the FDA PAT guideline, it was noted that merely switching from laboratory to process analytical methods does not constitute a PAT implementation that engenders process understanding.[12] Instead, systematic studies that incorporate modern process analyzers and sound experimental design are recommended in PAT endeavors; beginning from small laboratory scales to process development and scale-up, optimization, technology transfer, manufacturing production, and throughout the product life cycle.[12]

Another suite of tools that is vital for successful PAT applications contain multivariate data analysis methods that are generally classified under the scope of chemometrics.[13,20,21] A recent review highlighted "measuring or modeling a process variable" as one of the two major problems associated with chemical reaction scale-up.[22] This issue can be potentially resolved with the combination of in situ vibrational spectroscopy (infrared or Raman) and chemometrics numerical analyses, which were previously reported to be effective for reaction monitoring, determining kinetic rate contants, exploratory process development, and process control.[23−25]

In this contribution, an extended series of designed experiments using the model reaction of acetic anhydride hydrolysis were carried out from typical small laboratory scale glass vessels to medium-sized litre scale ones, to simulate the adoption of PAT during the early stages of laboratory bench and process development studies. Acetic anhydride hydrolysis kinetics have been

Received: December 22, 2010
Published: March 31, 2011

dx.doi.org/10.1021/op100337v | *Org. Process Res. Dev.* 2011, 15, 610–621

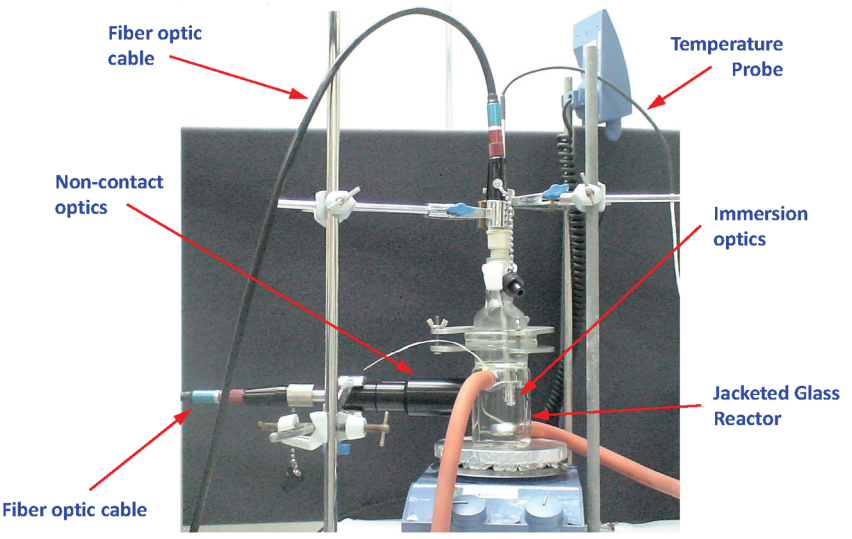

Figure 1. Typical lab-scale experimental setup with immersion (**C**) and noncontact (**NC**) in situ Raman optic.

previously investigated at typical laboratory scales by using a variety of analytical techniques such as titration, conductivity, calorimetry, and in situ optical spectrometry;[26−30] including ATR-FTIR,[28] Raman,[29] and UV-vis.[30] Several of these investigations also reported estimated reaction kinetics data. In this study, process Raman spectrometry was employed for in situ monitoring of the transient Raman spectra associated with the hydrolysis reaction. Both immersion and noncontact fiber optic probes were comparatively tested for each reaction run. Pertinent chemical information such as pure component spectra and transient concentration profiles were elucidated via various multivariate chemometrics post analyses. Finally, two different approaches were adopted for reaction kinetics modeling so as to engender process understanding. The first approach is the simple *Arrhenius model* while the second approach is a *dissolution-reaction model* that takes into account the effect of poor solubility of the acetic anhydride organic phase in water.

EXPERIMENTAL SECTION

A Kaiser RamanRXN3 process spectrometer was used for the experiments described in this work. The spectrometer utilizes holographic optical elements based on Volume Phase Technology (VPT) in an axial transmissive spectrograph configuration.[31] The RamanRXN3 uses an Invictus 785 nm near-infrared laser excitation with an average at source power set at 300 mW and was equipped with two separate fiber optic cables with different optical probe heads attached that could accommodate both contact/immersion and noncontact optics. Experimental spectra were obtained by using both types of in situ Raman monitoring techniques available, namely, immersion/contact optics with either 1/4 or 1/2 in. outer diameters (denoted herein as **C**) and a noncontact optics with 1.3 in. focal length (denoted herein as **NC**). A typical experimental setup for a laboratory bench-scale jacketed glass reactor is as shown in Figure 1. Regardless of the size or type of glass reactors (see below), the **C** and **NC** optics positions (i.e., at the sapphire crystal tip of the former and laser focal point of the latter) were respectively maintained at locations of 0.8 and 0.6 aspect ratios from the bottom of the reactor to the total liquid volume level. In situ Raman spectra were collected with single spectrum accumulation at 5 s exposure time, using a low-noise CCD detector thermoelectrically cooled to −40 °C. The time interval for switching between **C** and **NC** optics was 18 s, using the Kaiser multiplexing software *HoloPro*, in order to achieve near-simultaneous spectral acquisitions during reaction monitoring that reflect similar spectroscopic changes associated with acetic acid dissolution and hydrolysis kinetics at both monitoring optics. The Raman shift was recorded at 1 cm^{-1} Raman shift intervals for the range ca. 300−1950 cm^{-1}.

Three types of glass vessels were used in this study. Two of them are typically found in chemistry laboratories: the typical round-bottomed flask (RBF) and customized jacketed glass reactor (JGR) of sizes 50, 100, and 250 mL. Three other Lenz jacketed glass reactors of sizes 0.5, 1.0, and 3.0 L were also used. The 1/4 in. thick **C** optics was used for glass reactor size of 0.5 L or less, and the longer 1/2 in. thick **C** optics was used for 1.0 and 3.0 L vessels. For all the reactors ranging between 50 and 250 mL in volume, a Teflon coated magnetic bar stirrer was employed, with its rotational speed ρ_{rpm} (in rpm) was regulated by using a laboratory magnetic hot plate stirrer. The accuracy of the magnetic bar stirrer rotation speed was checked by using a light stroboscope. Because of the larger sizes of the 0.5, 1.0, and 3.0 L Lenz jacketed glass reactors, a pitch blade 45° angled impeller connected to an IKA stirrer motor was used.

Two series of kinetic studies were carried out: (i) stirring speed and reaction volume/vessel variation ρ_{rpm} (at constant $V_{reaction}$ and $T_{reaction}$), and (ii) variation in reaction temperature $T_{reaction}$ (at constant $V_{reaction}$ and ρ_{rpm}). The first series was primarily used for observing effects on acetic anhydride (AA) dissolution at low stirring speeds, whilst the second series was used for acquiring Raman spectral data for kinetics modeling and parameters estimation. Stirring speed was varied between $\rho_{rpm} = [100, 1000]$ rpm for the RBF and JGR laboratory bench-sized reactors of 250 mL size. For the 1.0 and 3.0 L Lenz reactors, the stirring speeds tested were 150, 300, 400, and 500 rpm. Poor AA dissolution was observed for the 150 rpm stirring run for the 1 L Lenz reactor and 100 rpm stirring for the smaller 50 and 250 mL reactors. For the 1 L Lenz reactor low stirring speed experiment, the denser AA phase was visibly observed to sink and form an organic layer at the bottom of the vessel due to the low solubility of AA in water. For stirring rates

dx.doi.org/10.1021/op100337v |*Org. Process Res. Dev.* 2011, 15, 610–621

of 300, 400, and 500 rpm in the 1.0 and 3.0 L vessel and also 700 and 1000 rpm in the small laboratory vessels, the stirring rates were adequate with no visible separation of organic and aqueous phases (which were corroborated by in situ Raman measurements). At these high stirring rates, the hydrolysis reaction was not influenced by AA dissolution problems, i.e. it progresses as reaction-controlled. As such, all further experiments for the second series of kinetic studies were carried out at 1000 rpm for 50 mL RBF and JGR vessels and 300 rpm for 0.5 L Lenz reactors. The experimental runs for 100 and 250 mL laboratory glass reactors and larger 1.0 and 3.0 L Lenz reactors were fixed at the constant temperature of 25 °C to compare their kinetics with those observed in the various 50 mL and 0.5 L glass vessels. Tables S1 and S2 (Supporting Information) provide a summary of the aforesaid experimental design.

A typical experiment begins with first filling the reactor with a fixed volume of distilled water and setting the reaction temperature. The initial water to AA mole ratio was maintained at ca. 47:1 for fixed volumes of reaction in different glass reactors. For example, this mole ratio is translated into appropriate water:AA volumes for total volumes V_{reaction} of 40, 80, and 200 mL conducted in 50, 100, and 250 mL vessels, respectively. For the Lenz jacketed reactors, V_{reaction} was maintained at 0.4, 0.8, and 2.4 L for the 0.5, 1.0, and 3.0 L vessels, respectively. Sufficient prereaction time was allowed for the distilled water to reach the desired temperature, T_{reaction}. Temperature control in jacketed reactors (JGR and Lenz) was maintained automatically by monitoring T_{reaction}, using a stainless steel temperature probe immersed into the reaction mixture before and throughout the hydrolysis. For RBF vessels, a mercury-based glass thermometer was used to manually maintain T_{reaction} by using heat supplied by an external oil bath in which the RBF was immersed. Once initial T_{reaction} of distilled water was stabilized, the predetermined volumetric quantity of AA was accurately dosed into the reactor by using either a Harvard syringe pump (for 50−250 mL reactor dosing) or a REGIO-Z/-2S pump (for 0.5−3.0 L reactor dosing). For experiment runs with 1000 rpm in RBF/JGR and 300 rpm in Lenz vessels, AA characteristic Raman peaks were observed to reach maximum intensity around ca. 2 min after dosing began. The AA dosing through different pump types, constant reaction temperature monitoring, and also the IKA stirrer speeds were controlled by in-house written LabVIEW software. Data collection of in situ Raman spectra with the Kaiser HoloPro software for both **NC** and **C** optics was simultaneously started when the AA dosing began for each experiment. Depending on the reaction temperature T_{reaction} and stirring rate used, the experimental time to complete the hydrolysis reaction is ca. 0.5 to 2.0 h.

■ MODELING AND COMPUTATIONAL ASPECTS

Multivariate Chemometrics. The Raman data acquired via RamanRXN3 spectrometer during in situ reaction monitoring intrinsically contain multispectroscopic wavelengths (i.e., Raman shift wavenumbers) for multireactions in the aforesaid experimental design. Thus, a multivariate approach must be adopted for its data analysis to elucidate pertinent chemical information for subsequent reaction kinetics modeling. In general, the set of Raman data collected for each experimental run can be denoted by a matrix $\mathbf{R}_{m\times\nu}$ with m number of time-dependent spectra and ν number of spectroscopic channels (Raman shift/wavenumber). Data for different optical probe types, that is immersion or noncontact, were separately analyzed as different optics contain different background Raman signals (see the next segment below). Alternatively, the Raman data for all reaction runs conducted for a particular reaction vessel type and optical probe can be collated together as a single large data array for chemometrics analysis. In the calculations herein, the former approach was chosen where each experimental run data was independently analyzed.

$$\mathbf{R}_{m\times\nu} = \mathbf{C}_{m\times s}\cdot\mathbf{r}^{\text{pure}}_{s\times\nu} + \mathbf{E}^{\text{spikes}}_{m\times\nu} + \mathbf{E}^{\text{residual}}_{m\times\nu} \quad (1)$$

The bilinear relationship between concentrations of Raman active chemical species and their corresponding pure component spectra[32,33] was relied upon for the multivariate chemometrics analyses herein. This bilinearity can be expressed as eq 1, which contains the multiplication of transient (time-dependent) concentration matrix and pure component spectra array of s number of Raman active chemical species observable during in- or online reaction monitoring.

The errors in this bilinear model of Raman data can be attributed to various sources, such as cosmic ray, container glass, and sample fluorescence.[34] Signal abberations (spikes) caused by cosmic rays, $\mathbf{E}^{\text{spikes}}_{m\times\nu}$, found in the measured Raman data were removed via an information-theoretic maximum entropy and minimum entropy (MaxEnt-MinEnt) cosmic ray "unspiking" algorithm written in-house.[35] The residual error $\mathbf{E}^{\text{residual}}_{m\times\nu}$ differs for the immersion and noncontact optical probes used. For the immersion probe, this residual error arises primarily from the Raman spectrum of the sapphire crystal tip of the probe.[7] An independent measurement of the immersion **C** probe placed in distilled water, $\vec{\mathbf{r}}^{\text{probe}}_{1\times\nu}$, was taken at the start of each experiment run so as to account for the residual error $\mathbf{E}^{\text{residual}}_{m\times\nu}$. For the **NC** optical probe, this spectral residual was primarily due to the Raman signals from the walls of the glass vessels used as reactors[34,36] and the thermal fluid passing through the jacketed vessel.

To account for the background Raman signal when using the **NC** probe, the following steps were taken before the start of each experimental run. First, the optimal **NC** probe distance from each glass vessel type was located, which produces Raman spectra with the *least background signal contributions* from both reactor glass and thermal fluid. Second, the **NC** probe is slightly shifted (a few millimeters) from this optimal position horizontally either nearer to or farther away from the outer glass vessel wall, and at each shifted location a Raman spectrum was measured to capture the different variations of the background Raman signals for each reactor vessel (see Figure S1, Supporting Information). The thermal fluid should be flowing through the glass jacket in this second step so as to capture Raman signals arising from the thermal fluid used (in this work water was used as thermal fluid, which has minimal Raman signals). Both the glass and thermal fluid Raman signals constitute a large part of the systematic errors found in $\mathbf{E}^{\text{residual}}_{m\times\nu}$. Roughly five spectra were acquired in this manner after the intended amount of distilled water was filled into each glass vessel before dosing in acetic anhydride. These background Raman spectra were subsequently collated into a data matrix $\mathbf{R}^{\text{bkgrd}}_{S\times\nu}$. This data matrix was subjected to singular value decomposition (SVD), which is similar to a principal component analysis (PCA), to obtain $\mathbf{V}^{\text{T}}$ vectors in its right singular matrix $\mathbf{V}^{\text{T}}_{\nu\times\nu}|_{\text{bkgrd}}$ according to eq 2. The initial 2−3 abstract $\mathbf{V}^{\text{T}}_{\text{bkgrd}}$ vectors obtained were found to effectively account for the residual Raman signal due to the glassware and thermal fluid. This method to account for $\mathbf{E}^{\text{residual}}_{m\times\nu}$ in **NC** optics was derived from a residual spectral analysis approach.[37] The position

of the **NC** probe was restored to the optimal location before starting the hydrolysis reaction by dosing in acetic anhydride.

$$\mathbf{R}^{\text{bkgrd}}_{5\times\nu} = \mathbf{U}_{5\times5}\Sigma_{5\times\nu}\mathbf{V}^{\text{T}}_{\nu\times\nu}|_{\text{bkgrd}} \quad (2)$$

$$\mathbf{R}_{m\times\nu} - \mathbf{E}^{\text{spikes}}_{m\times\nu} = \mathbf{R}^{\text{Unspiked}}_{m\times\nu} = \mathbf{U}_{m\times m}\Sigma_{m\times\nu}\mathbf{V}^{\text{T}}_{\nu\times\nu} \quad (3)$$

$$\vec{\mathbf{r}}^{\text{BTEM}}_{1\times\nu} = \vec{\mathbf{T}}_{1\times j}\cdot\mathbf{V}^{\text{T}}_{j\times\nu} \quad (4)$$

$$\hat{\mathbf{C}}^{\text{MLR}}_{m\times s} = \mathbf{R}^{\text{Unspiked}}_{m\times\nu}\cdot(\hat{\mathbf{r}}_{s\times\nu})^{\text{T}}\cdot[\hat{\mathbf{r}}_{s\times\nu}\cdot(\hat{\mathbf{r}}_{s\times\nu})^{\text{T}}]^{-1} \quad (5)$$

The pure component spectra of both acetic anhydride and acetic acid were recovered by using the band-target entropy minimization (BTEM) curve resolution algorithm.[38−40] BTEM reconstructs individual pure component spectra from their corresponding user-specified band-target, using generalized information entropy terms[40,41] that are based on various spectral vector properties.[41] This is in accordance with the *principle of simplicity*.[40,41] The cosmic spike removed data set $\mathbf{R}^{\text{Unspiked}}_{m\times\nu}$ for each experiment underwent SVD to obtain the right singular vectors in matrix $\mathbf{V}^{\text{T}}_{\nu\times\nu}$, eq 3. This $\mathbf{R}^{\text{Unspiked}}_{m\times\nu}$ matrix is equivalent to the first term after the equality sign in eq 1, that is, the multiplication of concentration matrix $\mathbf{C}_{m\times s}$ with pure component spectra matrix $\mathbf{r}^{\text{pure}}_{s\times\nu}$. Cosmic spike abberations had to be removed because they will influence the quality of recovered pure component spectra from multivariate curve resolution methods.[35] As written in eq 4, each BTEM estimate $\vec{\mathbf{r}}^{\text{BTEM}}_{1\times\nu}$ was resolved via optimizing for a transformation vector $\vec{\mathbf{T}}_{1\times j}$ via Corana's Simulated Annealing algorithm, using a basis vector space of j-th initial singular vectors $\mathbf{V}^{\text{T}}_{j\times\nu}$, where $1 \ll j < m$.[38−40] BTEM was previously demonstrated to be comparable, if not better, than other multivariate curve resolution methods such as IPCA, SIMPLISMA, and ALS based algorithms.[38,40]

As aforesaid, once the BTEM pure component spectral estimates of acetic anhydride and acetic acid were obtained, they were combined with either the $\vec{\mathbf{r}}^{\text{probe}}_{1\times\nu}$ spectrum or the initial 2−3 vectors $\mathbf{V}^{\text{T}}_{\text{bkgrd}}$ depending on whether the experimental data set was acquired from immersion **C** or noncontact **NC** optics. This consolidated spectral matrix $\hat{\mathbf{r}}_{s\times\nu}$ with s number of final spectral components accounts for Raman signals arising from reactant, product, and the spectral residual $\mathbf{E}^{\text{residual}}_{m\times\nu}$, with $\mathbf{E}^{\text{residual}}_{m\times\nu}$ represented by either *real* $\vec{\mathbf{r}}^{\text{probe}}_{1\times\nu}$ or *abstract* $\mathbf{V}^{\text{T}}_{\text{bkgrd}}$ vectors. That is, the s number of components in $\hat{\mathbf{r}}_{s\times\nu}$ include *real* spectra (from BTEM resolved component spectra or immersion **C** probe spectrum) and potentially *abstract* $\mathbf{V}^{\text{T}}$ vectors of reactor/thermal fluid background Raman signals (from using **NC** probe). The relative concentrations for acetic anhydride and acetic acid were estimated via a multilinear regression (MLR) by using pseudoinverse eq 5, which together with aforesaid Raman background signals forms the time-dependent matrix $\hat{\mathbf{C}}^{\text{MLR}}_{m\times s}$ corresponding to $\hat{\mathbf{r}}_{s\times\nu}$.[37] With the relative concentrations calculated, the kinetics for the acetic anhydride hydrolysis reaction can be modeled and kinetic rate constants estimated according to the two approaches delineated below.

Kinetics Modeling. The first reaction model assumes that the dissolution of acetic anhydride in water is fast at a sufficiently high rate of stirring with the reaction scheme proceeding as eq 6. Thus the second order rate equation to solve is eq 7, where AA denotes acetic anhydride for all the equations herein. By keeping the molar concentration of acetic anhydride low in comparison to water (ca. 1:47 mol ratio for all experiments herein), the reaction kinetics approximates a pseudo-first-order as shown in eq 8. The pseudo-first-order rate constant k at different isothermal reaction temperatures can be easily estimated by finding the gradient in eq 9. Since this equation involves the time-dependent dimensionless ratio $[\text{AA}]_t/[\text{AA}]_o$, the relative concentration values of AA found from MLR eq 5 suffices. Consequently, there is no requirement to perform calibrations to obtain the real (actual) concentration. Relative concentration data up to at least the second half-life of each hydrolysis run were used for estimating k. Subsequently, based on the Arrhenius theory,[42] the activation energy of hydrolysis, E_a, can be estimated from an exponential regression of eq 10.

$$(\text{CH}_3\text{CO})_2\text{O} + \text{H}_2\text{O} \rightarrow 2\text{CH}_3\text{COOH} \quad (6)$$

$$-\frac{\text{d}[\text{AA}]}{\text{d}t} = k'[\text{AA}][\text{H}_2\text{O}] \quad (7)$$

$$-\frac{\text{d}[\text{AA}]}{\text{d}t} = k[\text{AA}] \quad (8)$$

$$\ln\left(\frac{[\text{AA}]_t}{[\text{AA}]_o}\right) = -kt \quad (9)$$

$$k = k_o\exp(-E_a/RT) \quad (10)$$

Besides conducting the hydrolysis reactions at sufficiently high stirring rates, slow stirring rate experiments indicated that acetic anhydride is rather insoluble in water (see Figure 6 left plot; in particular the 100 rpm curve and the corresponding note on dissolution-reaction model in the Results and Discussion section). This insolubility has also been reported in the literature.[26] As such, a dissolution-reaction model was devised, with an assumed zeroth-order dissolution kinetics of eq 11 coupled to the revised hydrolysis reaction of eq 12, where the subscripts "(aq)" and "(organic)" denote chemical species in the aqueous and organic phases, respectively. The mathematical equations describing the dissolution-reaction model were separately solved for two concentration regimes. Since experimentally the molar ratio of AA to water was low, the pseudo-first-order reaction kinetics approximation for hydrolysis, eq 8, applies for both regimes with the previous rate constant k rewritten as $k_{\text{hydrolysis}}$ for clarity in eqs 13−15. In the first regime, where organic AA is present, that is $[\text{AA}_{(\text{organic})}] > 0$, the governing first-order ordinary differential equation is as eq 13, with its solution eq 14 found by using an integrating factor. The second concentration regime chronologically occurs after the first, in which all the organic phase AA has dissolved. As such, the exponential equation of eq 15 describes the rate of AA hydrolysis in the aqueous phase for the second regime.

$$(\text{CH}_3\text{CO})_2\text{O}_{(\text{organic})} \rightarrow (\text{CH}_3\text{CO})_2\text{O}_{(\text{aq})} \quad (11)$$

$$(\text{CH}_3\text{CO})_2\text{O}_{(\text{aq})} + \text{H}_2\text{O} \rightarrow 2\text{CH}_3\text{COOH}_{(\text{aq})} \quad (12)$$

$$\frac{\text{d}[\text{AA}_{(\text{aq})}]}{\text{d}t} = k_{\text{dissolution}} - k_{\text{hydrolysis}}[\text{AA}_{(\text{aq})}], \quad \forall\ [\text{AA}_{(\text{organic})}] > 0 \quad (13)$$

$$[\text{AA}_{(\text{aq})}] = \frac{k_{\text{dissolution}}}{k_{\text{hydrolysis}}}\{1 - \exp(-k_{\text{hydrolysis}}t)\} \quad (14)$$

$$[\text{AA}_{(\text{aq})}] = [\text{AA}_{(\text{aq})}]_o\exp(-k_{\text{hydrolysis}}t) \quad (15)$$

The dissolution and hydrolysis rate constants, $k_{\text{dissolution}}$ and $k_{\text{hydrolysis}}$, respectively, in both concentration regimes for each

dx.doi.org/10.1021/op100337v |*Org. Process Res. Dev.* 2011, 15, 610–621

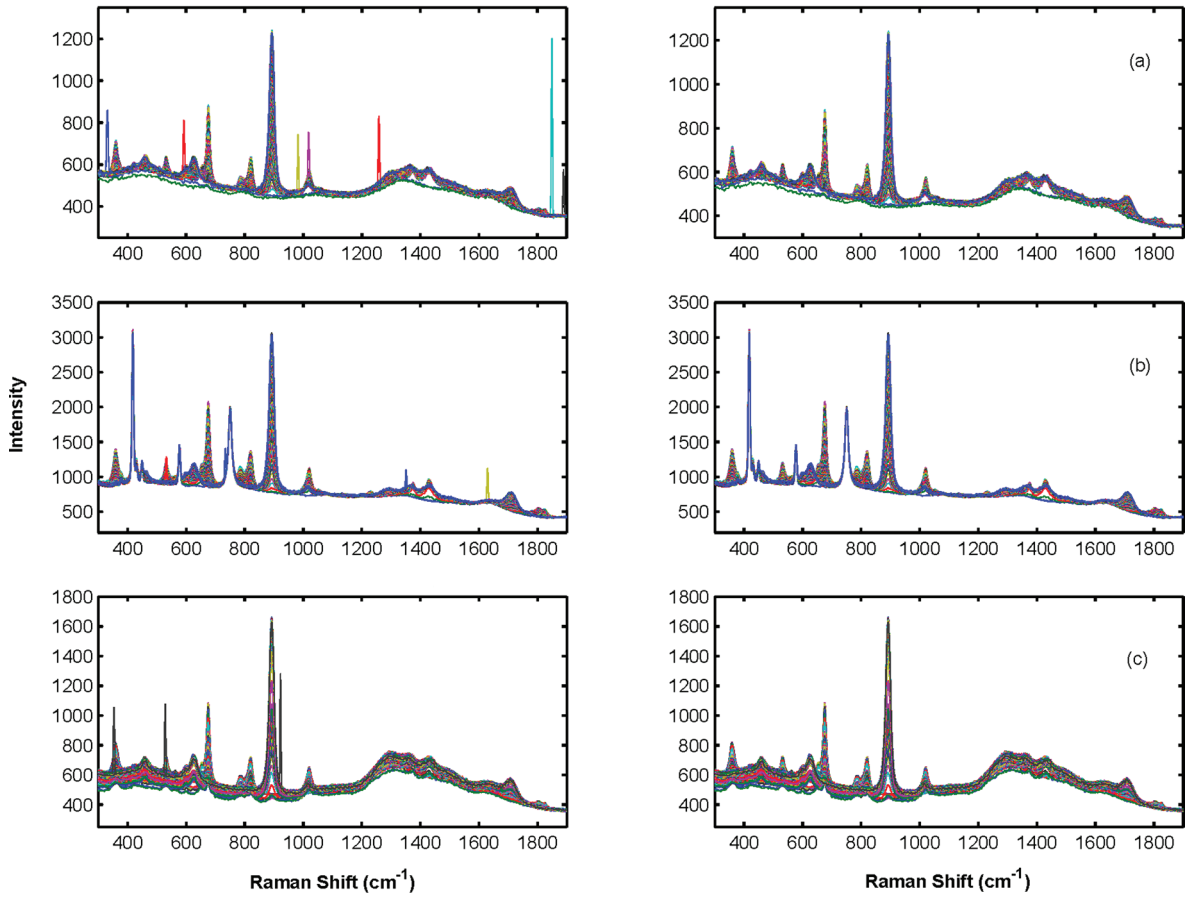

Figure 2. Representative removal of cosmic ray spike abberations, using the information-theoretic approach for reactor vessels of varied sizes. The subplots in the left column with sharp Raman spikes were effectively removed in their respective right column subplots. (a) 50 mL of JGR, noncontact optics, 20° reaction, (b) 250 mL of RBF, immersion optics, 25 °C reaction, (c) 3 L of Lenz, noncontact optics, 25 °C reaction.

experimental run were simultaneously estimated via a quasi-Newton numerical optimization algorithm, with an objective function that minimizes the difference between optimized simulation values $[AA_{(aq)}]$ and the time-dependent relative concentration values of AA in the aqueous phase (in matrix $\hat{\mathbf{C}}^{MLR}_{m\times s}$) obtained from chemometrics analyses of in situ Raman data. As with the aforesaid Arrhenius modeling, the actual AA concentration was not required (i.e., the time-dependent dimensionless ratio $[AA]_t/[AA]_o$ was utilized). A logical if-else construct was built into the quasi-Newton optimization program with use of Microsoft Excel 2007 to account for the two concentration regimes that physically occurred in each experimental data set, and the optimization based on eqs 13−15 was computed as a nonlinear problem by using tangent linear extrapolation estimation with first derivatives to estimate partial derivatives and nonnegativity constraint.

Computations. All chemometric analyses herein were developed by using in-house written scripts MATLAB version 7.3.0.267 (R2006b). The BTEM calculations were performed with in-house developed BTEM graphical user interface (GUI) software (version 1.0).[43] Multilinear regression (MLR) was performed with pseudoinverse[37] and the MaxEnt-MinEnt cosmic ray unspiking algorithm[35] were both executed by using MATLAB. The linear regressions and nonlinear optimizations for the Arrhenius theory and dissolution-reactions kinetics models were performed with Microsoft Excel 2007. All computations were carried out on an IBM computer running on Intel Pentium 4 CPU of 3.0 GHz, 512MB RAM with the Windows XP operating system.

RESULTS AND DISCUSSION

In situ Raman spectral data for each experimental run first underwent cosmic ray spike removal via an information-theoretic MaxEnt-MinEnt algorithm previously developed.[35] As shown in Figure 2, this MaxEnt-MinEnt cosmic ray unspiking program worked extremely well for all data obtained from different vessel types and sizes and through both **C** and **NC** optics. All Raman spike abberations of varied band shapes and wavenumber locations were automatically identified and removed within ca. 10 s of computational time, leaving behind "unspiked" Raman data that retain all genuine spectral band changes due to hydrolysis (compare Figure 2 left and right columns). The plots in Figure 2 also show that the spectral baselines for different glass vessels or different in situ Raman monitoring optics used do differ somewhat. For some of the experimental data sets, a minor baseline offset has to be made prior to executing the unspiking program in order to account for the baseline shift observed upon dosing in AA.

Once all cosmic ray spikes were removed, the band-target entropy minimization (BTEM) algorithm was utilized to resolve

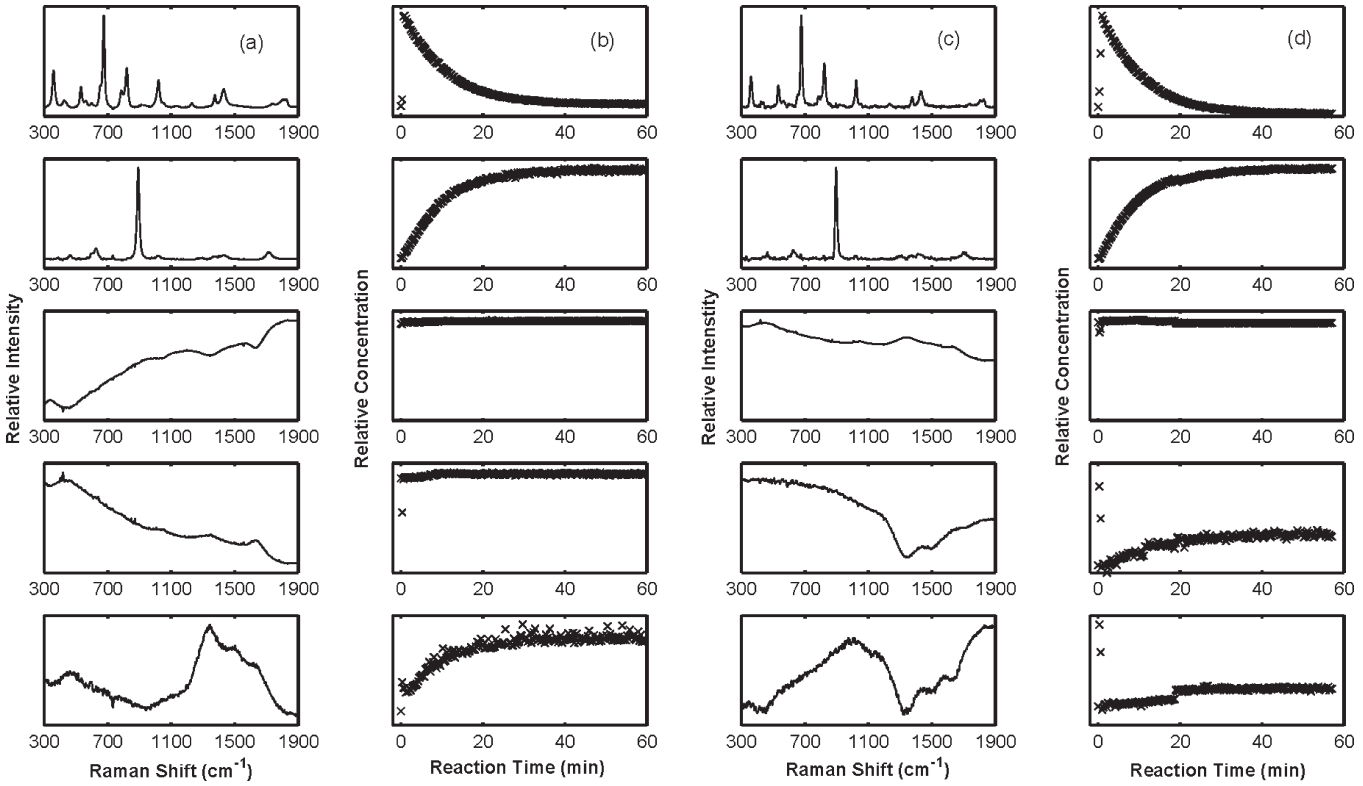

Figure 3. Multivariate curve resolution and multilinear regression of small lab-scale reactor vessels. RBF (50 mL) with noncontact optics for 25 °C reaction: (a) BTEM spectral estimates with abstract $\mathbf{V}^{T}$ vectors and (b) corresponding MLR relative concentration profiles. JGR (50 mL) with noncontact optics for 25 °C reaction: (c) BTEM spectral estimates with abstract $\mathbf{V}^{T}$ vectors and (d) corresponding MLR relative concentration profiles.

the pure component spectra of acetic anhydride and acetic acid. With these resolved chemical species spectra, the background spectrum of **C** optics probe $\vec{\mathbf{r}}^{\,\text{probe}}_{l\times\nu}$ or the abstract initial 2−3 singular vectors $\mathbf{V}^{T}_{\text{bkgrd}}$ from corresponding background Raman spectra combine to form $\hat{\mathbf{r}}_{s\times\nu}$. Subsequently, the relative spectral contributions of each chemical and background (real or abstract) Raman spectral component can be calculated by using multilinear regression (MLR) according to eq 5. Figure 3 (columns a and c, top two subplots) shows the BTEM resolved pure component estimates for AA and acetic acid, and their bottom three subplots are the three initial $\mathbf{V}^{T}_{\text{bkgrd}}$ vectors that accounted for the Raman background signals (from glass and thermal fluid) measured by using the **NC** probe from either 50 mL RBF or 50 mL JGR vessels. The subplots in columns b and d of Figure 3 are the MLR calculated transient relative concentration profiles corresponding to the spectrum in each row of Figure 3, columns a and c. The profiles of AA and acetic acid reflect typical reactant disappearance and product formation as reaction time progresses. Similarly, the top two subplots in columns a and c of Figure 4 belong to AA and acetic acid with their relative concentration profiles shown in Figure 4, columns b and d. The bottom two subplots in column a of Figure 4 are the two initial $\mathbf{V}^{T}_{\text{bkgrd}}$ vectors from Raman background signals, whereas the bottom subplot in column c of Figure 4 is that from the **C** probe $\vec{\mathbf{r}}^{\,\text{probe}}_{l\times\nu}$. Furthermore, the relative spectral contributions of the two chemical species in this model hydrolysis reaction are equivalent to their time-dependent relative concentrations, that is, noncalibrated arbitrary units. The AA and acetic acid BTEM spectral estimates in Figures 3 and 4 have excellent signal-to-noise ratio and corroborate well for all experiments in this work. Their corresponding transient relative concentration profiles obtained through MLR are thus useful for kinetic parameter estimation based on the aforesaid two theoretical kinetics models.

Figure 5 shows the various calculation results for the 0.5 L Lenz reactor **C** optics data, which are representative of similar computations herein that are based on the Arrhenius reaction kinetics model. The decrease in relative concentration of AA with reaction time is obtained from MLR, with all values for each reaction time series (i.e., experimental run) normalized with respect to corresponding maximum relative concentration value. As such, these normalized relative concentration values are equivalent to the time-dependent values of the dimensionless ratio $[AA]_t/[AA]_o$. The Arrhenius rate constant k in eq 9 for each reaction temperature T_{reaction} = [20, 40] is found by calculating the negative gradient of ln $([AA]_t/[AA]_o)$ with reaction time from the point where $[AA]_t/[AA]_o$ = 1.0 for at least the initial 2 half-lives in accordance with pseudo-first-order kinetics approximation of eq 9 (Figure 5, bottom left plot). That is, the initial AA dissolution lag time of ca. 2 min was not considered in this Arrhenius model, and the zero reaction time is referenced from the unity value for relative concentration rather than the start time of AA dosage. The linear regression R^2 value of these gradient calculations in all experimental runs averages around an excellent value of 0.989 for all **C** and **NC** temperature series data of 50 mL RBF, 50 mL JGR, and 0.5 L Lenz reactors. As demonstrated in the bottom

dx.doi.org/10.1021/op100337v |*Org. Process Res. Dev.* 2011, 15, 610–621

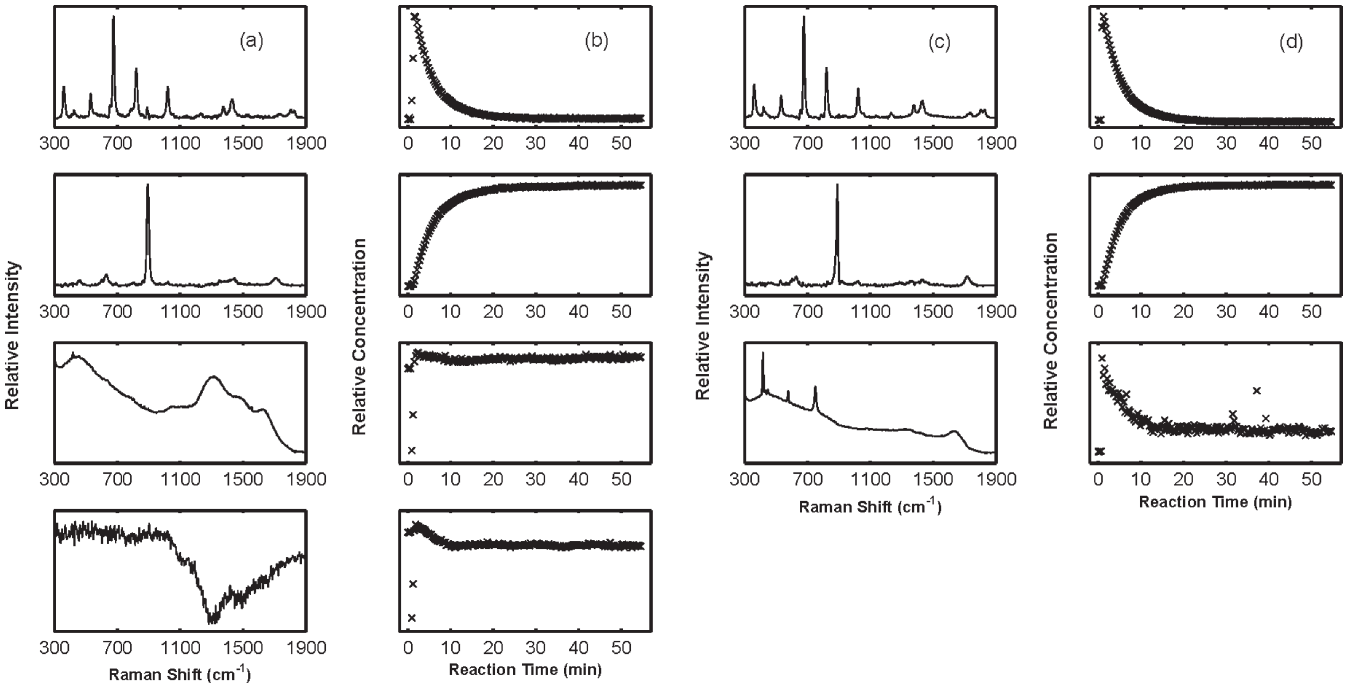

Figure 4. Multivariate curve resolution and multilinear regression of **NC** and **C** data from 0.5 L Lenz jacketed reactor vessel for 35 °C reaction: **NC** data (a) BTEM spectral estimates with abstract $\mathbf{V}^T$ vectors and (b) corresponding MLR relative concentration profiles, and **C** data (c) BTEM spectral estimates with immersion probe spectrum and (d) corresponding MLR relative concentration profiles.

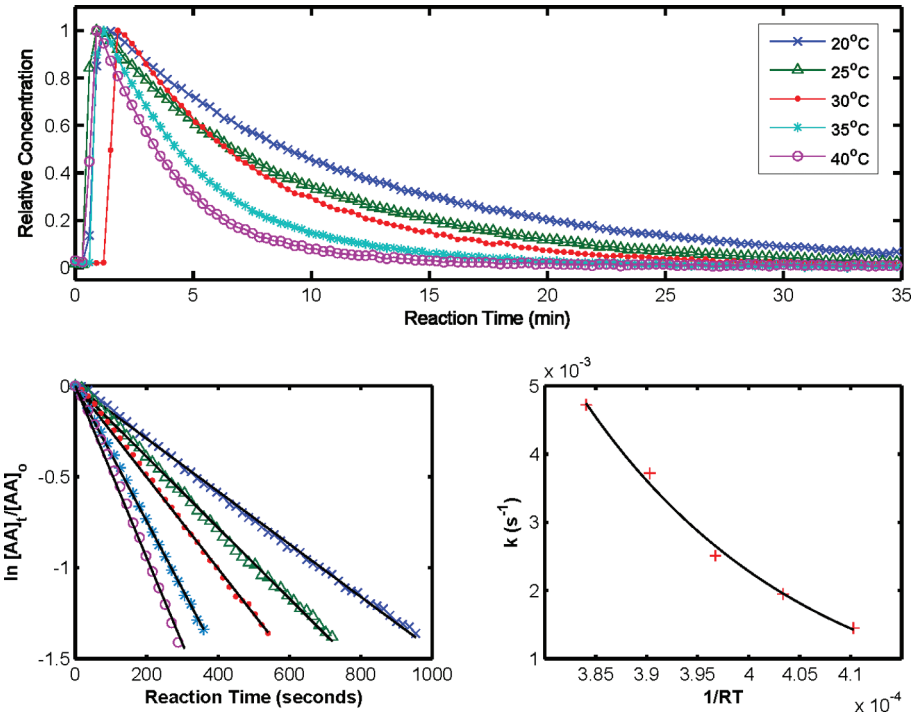

Figure 5. Representative graphical plots of Arrhenius model reaction kinetic parameters estimation for 0.5 L Lenz reactor **C** data. Top: Temperature-dependent relative concentration transient profiles from multilinear regression. Bottom left: Pseudo-first-order reaction kinetic constant estimation. Bottom right: Arrhenius model activation energy constant estimation.

right plot of Figure 5, the Arrhenius activation energy E_a for every glass reactor series is estimated by an exponential regression according to eq 10, and their average regression R^2 value is 0.981. The estimated Arrhenius model kinetic rate constant and activation energy values for the temperature series are given in Table 1.

dx.doi.org/10.1021/op100337v |*Org. Process Res. Dev.* 2011, 15, 610–621

For the dissolution-reaction kinetics model of eqs 13−15, $[AA]_t/[AA]_o$ data for reaction time range of ca. 20−35 min (depending on reaction temperature: longer reaction time ranges were selected for lower reaction temperatures, and all selected time ranges exceed beyond the second half-life stage for the dissolution-reaction modeling) underwent a nonlinear quasi-Newton optimization, using Microsoft Excel to generate optimal values for the dissolution and hydrolysis reaction kinetic constants. In contrast to the aforesaid pseudo-first-order Arrhenius model, this dissolution-reaction model includes the initial ca. 2 min of AA dissolution, i.e. assuming both dissolution and reaction begin at the start of AA dosage. The optimization objective is minimizing the sum of square errors (SSE) between simulated values calculated from solving eqs 13−15 and respective $[AA]_t/[AA]_o$ values. The left plot of Figure 6 shows the optimized relative concentration profiles (solid lines) overlaying the calculated $[AA]_t/[AA]_o$ values for 100, 300, and 1000 rpm stirring rates for three separate AA hydrolysis runs conducted at constant 25 °C in a 250 mL JGR, using the **NC** optics for Raman monitoring. The numerical fit with the proposed dissolution-reaction model is very good, with the two aforesaid concentration regimes of this hybrid kinetics model well accounted. The same optimization strategy was subsequently applied to other experimental runs, and yield equally good numerical fit. The right plot of Figure 6 demonstrates the fitting between simulated (solid lines) values obtained through the same nonlinear optimization and experimentally calculated transient values of $[AA]_t/[AA]_o$ from BTEM-MLR computations for the temperature series of AA hydrolysis in 50 mL JGR using **C** data. The estimated dissolution and hydrolysis rate constants of this hybrid model for the temperature series experiments in this study are shown in Tables 2 and 3.

The aforesaid numerical treatments for the pseudo-first-order reaction kinetics and dissolution-reaction models were applied to the stirring speed and reaction volume/vessels variation

Table 1. Apparent Pseudo-First-Order Rate Constants and Arrhenius Parameters of Acetic Anhydride Hydrolysis[a]

	RBF 50 mL		JGR 50 mL		Lenz 0.5 L	
reaction temp (°C)	C	NC	C	NC	C	NC
20	1.548	1.149	1.267	1.311	1.441	
25	1.872	1.590	1.707	1.645	1.940	2.100
30	2.366	2.062	2.422	2.449	2.505	2.600
35	3.357	3.073	3.081	3.050	3.720	3.500
40	3.715	2.965	3.915	3.683	4.789	4.800
ln (k_o)	8.133	9.339	11.187	10.187	12.549	11.172
E_a (kJ/mol)	35.648	39.147	43.494	41.006	46.582	43.060

[a] First-order reaction rate constant k (10^{-3} s^{-1}) calculated for at least the initial 2 half-lives.

Table 2. Optimized Apparent Hydrolysis Rate Constants of Acetic Anhydride from Dissolution-Reaction Model[a]

	RBF 50 mL		JGR 50 mL		Lenz 0.5 L	
reaction temp (°C)	C	NC	C	NC	C	NC
20	1.599	1.063	1.256	1.416	1.416	
25	2.043	1.541	1.725	1.585	1.870	1.936
30	2.413	1.829	2.392	2.278	2.482	2.458
35	3.335	2.957	3.047	2.916	3.478	3.485
40	3.720	2.466	3.810	3.866	4.755	4.850

[a] Hydrolysis rate constant $k_{hydrolysis}$ (10^{-3} s^{-1}) monitored via in situ Raman spectroscopy.

Table 3. Optimized Apparent Dissolution Rate Constants of Acetic Anhydride from Dissolution-Reaction Model[a]

	RBF 50 mL		JGR 50 mL		Lenz 0.5 L	
reaction temp (°C)	C	NC	C	NC	C	NC
20	5.636	1.248	5.402	2.495	2.495	
25	2.529	4.202	3.200	1.623	0.885	10.50
30	2.000	4.637	1.834	5.556	1.990	2.866
35	1.656	2.119	1.413	1.065	0.880	5.007
40	1.460	2.254	1.171	1.481	0.781	5.556

[a] Dissolution rate constant $k_{dissolution}$ (10^{-3} s^{-1}) monitored via in situ Raman spectroscopy.

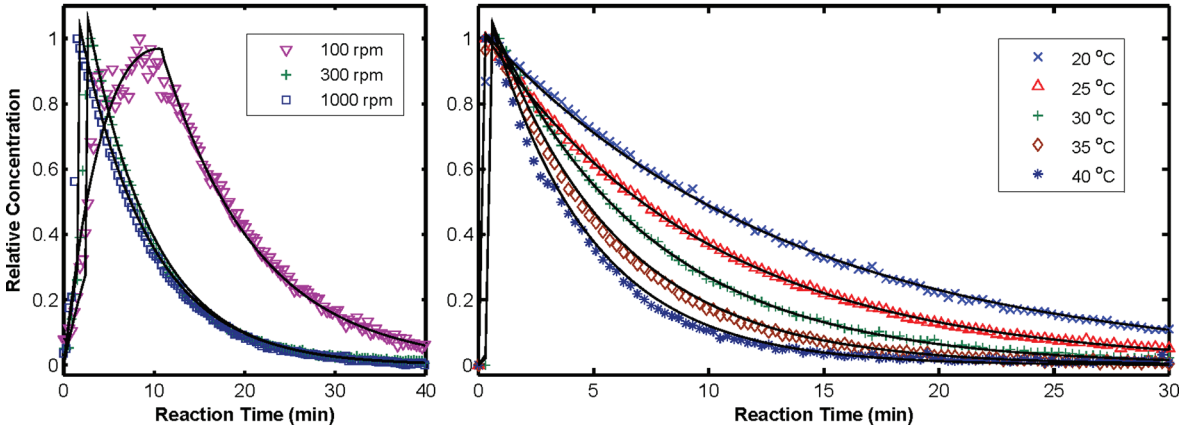

Figure 6. Representative graphical plots of transient AA relative concentration profiles from dissolution-reaction model kinetic parameters estimation (data points from analyses of experimental Raman spectra; solid lines from quasi-Newton numerical optimization). Left plot: Different stirring rates at constant temperature 25 °C. Right plot: Different reaction temperatures at constant 1000 rpm stirring rate.

dx.doi.org/10.1021/op100337v |*Org. Process Res. Dev.* 2011, 15, 610–621

Table 4. Apparent Reaction Rate Constants for Pseudo-First-Order Initial Reaction Rate Approximation (Arrhenius Theory) and Optimized Hydrolysis Rate (Dissolution-Reaction Model) of Various Reactor Vessels at Different Stirring Speeds (At Constant Reaction Temperature 25 °C)[a]

stirring speed (rpm)	RBF 50 mL	JGR 50 mL	RBF 100 mL	JGR 100 mL	RBF 250 mL	JGR 250 mL	Lenz 0.5 L	Lenz 1.0 L	Lenz 3.0 L
immersion/contact (C) optics									
100					2.473 (2.228)	9.728 (0.776)			
150							0.581 (1.186)	0.590 (1.140)	
300					2.508 (2.331)	1.764 (1.771)	1.866 (1.822)	1.866 (1.821)	1.847 (1.544)
400									2.105 (2.005)
500							1.949 (1.933)	1.949 (1.931)	2.267 (2.023)
700					2.265 (2.221)	1.800 (1.768)			
1000	1.872 (2.043)	1.707 (1.725)	2.091 (2.102)	1.824 (1.719)	2.099 (2.126)	1.709 (1.810)			
noncontact (NC) optics									
100					2.447 (2.235)	1.264 (1.319)			
150							1.729 (1.142)	0.607 (1.137)	
300					2.369 (2.274)	1.762 (1.690)	1.825 (1.758)	1.829 (1.663)	2.985 (2.912)
400									2.230 (1.972)
500							2.053 (1.909)	2.053 (1.928)	2.231 (2.238)
700					2.195 (2.128)	1.771 (1.735)			
1000	1.590 (1.541)	1.645 (1.585)	1.939 (1.817)	1.966 (1.728)	2.094 (2.169)	1.731 (1.805)			

[a] First-order reaction rate constants k (10^{-3} s^{-1}) calculated for at least the initial 2 half-lives; optimized hydrolysis rate constants $k_{hydrolysis}$ (10^{-3} s^{-1}) given within parentheses.

Table 5. Apparent Dissolution Rate Constants (Dissolution-Reaction Model) for Different Reactor Vessels at Different Stirring Speeds (At Constant Reaction Temperature 25 °C)[a]

stirring speed (rpm)	RBF 50 mL	JGR 50 mL	RBF 100 mL	JGR 100 mL	RBF 250 mL	JGR 250 mL	Lenz 0.5 L	Lenz 1.0 L	Lenz 3.0 L
immersion/contact (C) optics									
100					2.632	7.684			
150							3.797	1.938	
300					4.471	7.046	6.481	6.288	1.755
400									3.101
500							7.096	7.258	2.215
700					5.962	8.942			
1000	2.529	3.200	1.425	1.557	5.962	2.092			
noncontact (NC) optics									
100					2.656	3.975			
150							3.005	1.937	
300					2.235	4.794	4.167	8.060	8.998
400									1.939
500							5.556	5.091	1.410
700					3.577	4.514			
1000	4.202	1.623	1.526	8.088	3.577	5.556			

[a] Optimized acetic anhydride dissolution rate constants $k_{dissolution}$ (10^{-3} s^{-1}).

experiments and their optimized kinetics parameter estimates are presented in Tables 4 and 5. The estimated value for the first-order initial reaction rate (Arrhenius theory) is stated side by side with that for the optimized hydrolysis rate (dissolution-reaction model) for each reaction conducted, with the latter given within parentheses.

Several pieces of information can be inferred from the pseudo-first-order approximation and estimated Arrhenius model parameters (see Table 1 and Figure 5). The pseudo-first-approximation rate constants and Arrhenius model yield excellent regression estimates with k, $\ln(k_o)$, and E_a values comparable to those reported in the literature.[26,30] Furthermore, these values were determined by applying aforesaid multivariate analyses, in contrast to using the single wavelength/wavenumber (univariate) method.[30] As given in Table S3 (Supporting Information), the pseudo-first-order rate constants between **C** and **NC** data of smaller 50 mL vessels of RBF and JGR differ more at the two ends of the reaction temperature range (i.e., 20 and 40 °C), with the RBF difference ranging from 8.45% to 25.79% and the JGR differing only between 1.01% and 5.93%. For the Lenz 0.5 L temperature series the deviation is

1.18−9.14%, with its **NC** data at 20 °C not representative due to observed condensation of water vapour on the reactor outer wall at this low reaction temperature (no repetition of this 20 °C experiment was done). Besides this data set outlier, the other values in both **C** and **NC** data for the 0.5 L Lenz vessel yield comparable rate constants. Another outlier **NC** data found was that of 50 mL RBF at 40 °C temperature. As shown in Figure S2 (Supporting Information), the $[AA]_t/[AA]_o$ and $\ln([AA]_t/[AA]_o)$ values obtained from **NC** data were scattered for the experiment of 50 mL RBF at 40 °C, which is a significant contrast from its **C** data counterpart. Therefore, though numerical calculations can be performed on the data from 50 mL RBF at 40 °C, the **NC** data rate constant was not following the same trend of its corresponding **C** data. The general observations just described for the pseudo-first-order approximation are similar for the optimized hydrolysis reaction rates (see Table 2).

The comparison of optimized hydrolysis reaction rate (dissolution-reaction model) and pseudo-first-order rate constants (Arrhenius theory) was made by calculating their average percentage deviation, which is given in Table S4 (Supporting Information). For the **C** data, both 50 mL RBF and 0.5 L Lenz reactors have an average of ca. 2.8% difference between the two kinetic models, whereas for 50 mL JGR it is only ca. 1.4%. For corresponding **NC** data, the dissimilarity decreases from around 9.36% (50 mL RBF), 5.6% (50 mL JGR) to 3.7% (0.5 L Lenz). Overall, the difference between these two models was not very significant for the temperature series experiments. Since good stirring rates were maintained for these temperature series experiments, their corresponding Raman spectral data sets reflected reaction-controlled rather than AA dissolution-controlled scenarios.

The strength of using the relatively more sophisticated dissolution-reaction model can be seen in the comparison of reaction rate constants at isothermal 25 °C across different stirring speeds with various glass vessel types (see Tables 4 and 5). As aforementioned, this is to mock up systematic kinetics studies that occur during process development, in which new reactions are investigated through various reaction volumes and vessels, using different stirring rates and regimes to find optimal large-scale process operation parameters. From Tables 1 and 2, the reaction rates for 25 °C hydrolysis runs in three different vessels (50 mL RBF, 50 mL JGR, and 0.5 L Lenz) spread over 1.541×10^{-3} to 2.100×10^{-3} s^{-1} with an average value of ca. 1.796×10^{-3} s^{-1}. This serves as a benchmark average value for comparing the reaction rates obtained for the stirring speed and reaction volume variations studies. For the experimental runs with stirring speeds of 400 rpm and above in Table 4, the spread of reaction rates ranges is 1.541×10^{-3} to 2.238×10^{-3} s^{-1} (**NC** data) and 1.707×10^{-3} to 2.267×10^{-3} s^{-1} (**C** data), with averages of 1.919×10^{-3} and 1.960×10^{-3} s^{-1}, respectively. Out of these 24 hydrolysis runs, two-thirds of the estimated pseudo-first-order reaction rates are slightly higher than corresponding optimized rates obtained from the dissolution-reaction model, with average percentage differences of 0.74% (**C** data) and 3.89% (**NC** data) between the two kinetics models. Taking the benchmark value of 1.796×10^{-3} s^{-1}, the **C** data deviates by an average of 9.66% (pseudo-first-order) and 8.59% (dissolution-reaction), whilst the corresponding **NC** data deviates by 9.02% (pseudo-first-order) and 4.64% (dissolution-reaction). A similar comparison using the reaction rates in Table 4 for stirring speeds of 300 rpm or less yield more striking findings. Their spread of reaction rates spans 0.607×10^{-3} to 2.985×10^{-3} s^{-1} (**NC** data) and 0.581×10^{-3} to 9.728×10^{-3} s^{-1} (**C** data), with averages of 1.830×10^{-3} and 2.102×10^{-3} s^{-1}, respectively. Abnormally diverse reaction rates such as 0.607×10^{-3} s^{-1} or even 9.728×10^{-3} s^{-1} were obtained due to the shift of reaction-controlled regime to dissolution-controlled regime at low stirring rates, especially at 150 or 100 rpm. The left plot in Figure 6 shows the comparison between fast and slow dissolution relative concentration profiles resulting from the different stirring speeds. Contrasting with the benchmark value of 1.796×10^{-3} s^{-1}, the **C** data deviate by an absolute average of 43.66% (pseudo-first-order) and 9.57% (dissolution-reaction), whereas correspondingly the **NC** data deviate by 4.03% (pseudo-first-order) and 0.22% (dissolution-reaction). In summary, the differential equations in the dissolution-reaction model describing two distinct regimes during AA hyrolysis phenomenon provided a means to correct the errors arising from poor dissolution; albeit this is a partial numerical rectification rather than a full physicochemical theoretical treatment.

Between using immersion (**C**) and noncontact (**NC**) optics for in situ Raman spectroscopy, there appears to be a slight advantage in using the former. In the temperature series experiments, the larger deviation found in the **NC** data of RBF could be due to better temperature control and strirring rates maintained in the jacketed JGR and Lenz reactors in contrast to the RBF. The conditions near the sapphire crystal of the immersion optics and the laser focal point of the noncontact optics differ more for the RBF.

Moreover, noncontact optics measurements can be impeded by condensation that occurs on outer reactor walls for low-temperature studies (especially in environments with high atmospheric humidity), and the glass Raman scatter background has to be compensated (see Figure S1, Supporting Information). Figure S3 (Supporting Information, left bottom image) shows water vapour condensation on the reactor outer wall for a hydrolysis conducted at 15 °C. Furthermore, the quantitative results obtained in this study indicate more consistent measurements from the **C** data compared to **NC**. At adequate stirring speeds that favor the reaction-controlled regime, the deviation of hydrolysis reaction rates between the two kinetics modeling approaches is slightly lower for the **C** data, reflecting the spectroscopic complications that are associated with the noncontact optics method. Apart from these slight differences, the present work demonstrated that the kinetics parameter estimations obtained from noncontact optics is in very good agreement with those of immersion optics.

The immersion optics is not without drawbacks. At times when there are bubbles surrounding the sapphire crystal tip of the immersion optics during AA hydrolysis, these bubbles will obstruct Raman measurements (see Figure S3, Supporting Information, right top image). Such untimely obstructions will cause anomalies to both the Raman spectra and their regressed transient concentration data points as shown in Figure S3 (Supporting Information, left top image). A similar analytical impasse can be anticipated during monitoring of multiphase systems, e.g. crystallization, suspensions, slurry, gas-liquid, etc., if Raman immersion optics is employed. When deploying in situ Raman spectroscopy for real-time process monitoring and on-the-flight chemometrics analysis, the aforesaid Raman spectroscopic anomalies arising from abnormal physical situations for noncontact and immersion optics has to be intelligently dealt with by using appropriate numerical algorithms in order not to raise premature alarms that erroneously signify process failure.

CONCLUSION

The combination of in situ Raman monitoring, information-theoretic multivariate chemometrics, and kinetics modeling

approaches was demonstrated herein to be effective for generating better process understanding of the acetic anhydride model reaction during process development. The similarities and differences in spectroscopic measurements (immersion and noncontact optics), data processing (cosmic ray aberrations removal, accounting for spectral anormalies and glass vessel background, and sapphire crystal of probe), multivariate analysis (curve resolution and data regression), use of different reaction volumes in varied glass reactors, and their estimated kinetics modeling parameters (pseudo-first-order reaction, Arrhenius theory, and dissolution-reaction kinetics) were studied and discussed.

Pertinent chemical process information encoded within the recorded in situ Raman data were decoded, i.e. unraveled, via the sequence of chemometrics analyses and explained through postulated kinetics models. The estimated pseudo-first-order hydrolysis rate constants and Arrhenius theory parameters were consistent with those previously reported in the literature, and the dissolution-reaction model provided a means for partially correcting the hydrolysis rate constants of experiments at low stirring speeds. Both noncontact and immersion probe optics were comparable for measuring in situ Raman spectra and reflecting hydrolysis rates under well-mixed reaction-controlled conditions, but each has its advantages and shortfalls that should be considered in actual deployment. The overall protocol described in this work, which connects in situ analytical measurements, multivariate chemometrics, and kinetics modeling, can serve as a general methodology for studies of novel chemistries in process development.

■ ASSOCIATED CONTENT

Supporting Information. Tables S1−S9 (summary of stirring speed variation experiments; summary of temperature variation experiments; percentage deviation of estimated pseudo-first-order rate constants (Arrhenius theory) between **C** and **NC** optics data; average percentage deviation of estimated pseudo-first-order and optimized hydrolysis rate constants; pseudo-first-order rate constants and Arrhenius parameters of acetic anhydride hydrolysis; optimized hydrolysis apparent rate constants of acetic anhydride from the dissolution-reaction model; optimized dissolution apparent rate constants of acetic anhydride from the dissolution-reaction model; reaction rate constants for pseudo-first-order initial reaction rate approximation (Arrhenius theory) and optimized apparent hydrolysis rate (dissolution-reaction model) for different reactor vessels at different stirring speeds (constant reaction temperature 25 °C); and apparent dissolution rate constants (dissolution-reaction model) for different reactor vessels at different stirring speeds, respectively) and Figures S1−S3 (Background Raman spectra of immersion probe optics and various jacketed glass reactors; comparison of C and NC data for the hydrolysis experiment at 40 °C in 50 mL of RBF; and Raman in situ optics problems associated with physical experimental setup conditions, respectively). This material is available free of charge via the Internet at http://pubs.acs.org.

■ AUTHOR INFORMATION

Corresponding Author

*Phone: (65) 6796 3961. Fax: (65) 6316 6185. E-mail: chew_wee@ices.a-star.edu.sg.

■ ACKNOWLEDGMENT

The authors would like to express gratitude to the Institute of Chemical and Engineering Sciences (ICES) for research funding support through an industrial collobration project ICES/06-330B01 with National Instruments. The cosmic ray unspiking algorithm employed herein[35] was developed through the same industrial project. The authors also thank Professor Brian Cox of AstraZeneca for his invaluable input for developing the dissolution-reaction kinetics model and related numerical optimization.

■ REFERENCES

(1) Lewis, I. R.; Edwards, H. G. M., Eds. *Handbook of Raman Spectroscopy*; Marcel Dekker: New York, 2001.

(2) Gremlich, H.-U.; Yan, B., Eds. *Infrared and Raman Spectroscopy of Biological Materials*; Marcel Dekker: New York, 2001.

(3) Chalmers, J. M.; Griffiths, P. R., Eds. *Handbook of Vibrational Spectroscopy*; John Wiley & Sons Ltd: West Sussex, UK, 2002.

(4) Kiefer, W. *J. Raman Spectrosc.* **2007**, *38*, 1538.

(5) Raman, C. V.; Krishnan, K. S. *Nature* **1928**, *121*, 501.

(6) Landsberg, G.; Mandelstam, L. *Naturwissenschaften* **1928**, *16*, 557.

(7) Lewis, I. R.; Lewis, M. L. In *Handbook of Vibrational Spectroscopy*; Chalmers, J. M., Griffiths, P. R., Eds.; John Wiley & Sons Ltd: West Sussex, UK, 2002; Vol. 2, Fiber-optic Probes for Raman Spectrometry, p 1587.

(8) Adar, F. In *Handbook of Raman Spectroscopy*; Lewis, I. R., Edwards, H. G. M., Eds.; Marcel Dekker: New York, 2001; Chapter 2, Evolution and Revolution of Raman Instrumentation - Application of Available Technologies to Spectroscopy and Microscopy, p 11.

(9) Slater, J. B.; Tedescon, J. M.; Fairchild, R. C.; Lewis, I. R. In *Handbook of Raman Spectroscopy*; Lewis, I. R., Edwards, H. G. M., Eds.; Marcel Dekker: New York, 2001; Chapter 3, Raman Spectrometry and Its Adaptation to the Industrial Environment, p 41.

(10) Lewis, I. R. In *Handbook of Raman Spectroscopy*; Lewis, I. R., Edwards, H. G. M., Eds.; Marcel Dekker: New York, 2001; Chapter 23, Process Raman Spectroscopy, p 919.

(11) Jestel, N. L. In *Process Analytical Technology: Spectroscopic Tools and Implementation Strategies for the Chemical and Pharmaceutical Industries*; Bakeev, K. A., Ed.; Blackwell Publishing: Oxford, UK, 2005; Chapter 5, Process Raman Spectroscopy, p 133.

(12) U.S. Department of Health and Human Services. Food and Drug Administration (FDA), Center for Drug Evaluation and Research (CDER), Center for Veterinary Medicine (CVM), Office of Regulatory Affairs (ORA), *Guidance for Industry PAT − A Framework for Innovative Pharmaceutical Manufacturing and Quality Assurance (Draft Guidance)*, September 2004.

(13) Chew, W.; Sharratt, P. *Anal. Methods* **2010**, *2*, 1412.

(14) Everall, N.; Clegg, I.; King, B. In *Handbook of Vibrational Spectroscopy*; Chalmers, J. M., Griffiths, P. R., Eds.; John Wiley & Sons Ltd: West Sussex, UK, 2002; Vol. 4, Process Measurements by Raman Spectroscopy, p 2770.

(15) Williams, A. C. In *Handbook of Raman Spectroscopy*; Lewis, I. R., Edwards, H. G. M., Eds.; Marcel Dekker: New York, 2001; Chapter 14, Some Pharmaceutical Applications of Raman Spectroscopy, p 575.

(16) Gendrin, C.; Roggo, Y.; Collet, C. *J. Pharm. Biomed. Anal.* **2008**, *48*, 533.

(17) U.S. Department of Health and Human Services. Food and Drug Administration, *Phamaceutical CGMPs for the 21st Century − A Risk-Based Approach. Final Report*, September 2004.

(18) European Medicines Agency (EMA), *PAT Team Reflection Paper: Chemical, pharmaceutical and biological information to be included in dossiers when Process Analytical Technology (PAT) is employed*, March 2006, http://www.emea.europa.eu/Inspections/docs/PATGuidance.pdf.

(19) Garcia, T.; Cook, G.; Nosal, R. *J. Pharm. Innov.* **2008**, *3*, 60.

(20) Miller, C. E. In *Process Analytical Technology: Spectroscopic Tools and Implementation Strategies for the Chemical and Pharmaceutical*

Industries; Bakeev, K. A., Ed.; Blackwell Publishing: Oxford, UK, 2005; Chapter 8, Chemometrics in Process Analytical Chemistry, p 226.
(21) Wold, S.; Cheney, J.; Kettaneh, N.; McCready, C. *Chemom. Intell. Lab. Syst.* **2006**, *84*, 159.
(22) Caygill, G.; Zanfir, M.; Gavriilidis, A. *Org. Process Res. Dev.* **2006**, *10*, 539.
(23) Cooper, J. B. *Chemom. Intell. Lab. Syst.* **1999**, *46*, 231.
(24) Svensson, O.; Josefson, M.; Langkilde, F. W. *Chemom. Intell. Lab. Syst.* **1999**, *49*, 49.
(25) Miller, C. E. *J. Chemom.* **2000**, *14*, 513.
(26) Hirota, W. H.; Rodrigues, R. B.; Sayer, C.; Guidici, R. *Chem. Eng. Sci.* **2010**, *65*, 3849.
(27) Shatynskit, J. J.; Hanesian, D. *Ind. Eng. Chem. Res.* **1993**, *32*, 594.
(28) Zogg, A.; Fischer, U.; Hungerbuhler, K. *Chemom. Intell. Lab. Syst.* **2004**, *71*, 165.
(29) Bell, W. C.; Booksh, K. S.; Myrick, M. L. *Anal. Chem.* **1998**, *70*, 332.
(30) Ampelli, C.; Bella, D; Lister, D.; Maschio, G.; Parisi, J. *J. Therm. Anal. Calorim.* **2003**, *72*, 875.
(31) *RamanRXN3 operations manual*, version 5.0, Kaiser Optical Systems Inc., 2005.
(32) Jiang, J.-H.; Liang, Y.; Ozaki, Y. *Chemom. Intell. Lab. Syst.* **2004**, *71*, 1.
(33) Tan, S.-T.; Zhu, H.; Chew, W. *Anal. Chim. Acta* **2009**, *639*, 29.
(34) Bowie, B. T.; Chase, D. B.; Lewis, I. R.; Griffiths, P. R. In *Handbook of Vibrational Spectroscopy*; Chalmers, J. M., Griffiths, P. R., Eds.; John Wiley & Sons Ltd: West Sussex, UK, 2002; Vol. 3, Anomalies and Artifacts in Raman Spectroscopy, p 2355.
(35) Chew, W. *J. Raman Spectrosc.* **2011**, *42*, 36.
(36) Carabatos-Nédelec, C. In *Handbook of Raman Spectroscopy*; Lewis, I. R., Edwards, H. G. M., Eds.; Marcel Dekker: New York, 2001; Chapter 10, Raman Scattering of Glass, p 423.
(37) Kee, B. H.; Sim, W.-S.; Chew, W. *Anal. Chim. Acta* **2006**, *571*, 113.
(38) Chew, W.; Widjaja, E.; Garland, M. *Organometallics* **2002**, *21*, 1982.
(39) Widjaja, E.; Li, C.; Garland, M. *Organometallics* **2002**, *21*, 1991.
(40) Widjaja, E.; Li, C.; Chew, W.; Garland, M. *Anal. Chem.* **2003**, *75*, 4499.
(41) Tan, S.-T.; Chen, K.; Ong, S.; Chew, W. *Analyst* **2008**, *133*, 1395.
(42) Espensen, J. H. *Chemical Kinetics and Reaction Mechanisms*, 2nd ed.; McGraw-Hill, Inc.: Singapore, 1995.
(43) Ong, S.; Ong, C. S. S.; Jiang, A.; Chew, W.; Zhang, H.; Widjaja, E.; Li, C.; Chen, L.; Garland, M. *Band-Target Entropy Minimization Graphical User Interface (GUI) Software*, version 1.0, 2005−2008; Institute of Chemical and Engineering Sciences (ICES); Agency of Science, Technology and Research (A*STAR), Singapore; National University of Singapore.